Strain-Driven Dzyaloshinskii-Moriya Interaction for Room-Temperature Magnetic Skyrmions

Yuelin Zhang,[1,*] Jie Liu,[1,6,*] Yongqi Dong,[2,*] Shizhe Wu,[1,*] Jianyu Zhang,[3,*] Jie Wang,[1] Jingdi Lu,[1] Andreas Rückriegel,[4,5] Hanchen Wang,[3] Rembert Duine,[4,5] Haiming Yu[3,†] Zhenlin Luo,[2,‡] Ka Shen[1,6,§] and Jinxing Zhang[1,‖]

[1]*Department of Physics, Beijing Normal University, Beijing 100875, China*
[2]*National Synchrotron Radiation Laboratory, University of Science and Technology of China, Hefei, Anhui 230026, China*
[3]*Fert Beijing Institute, MIIT Key Laboratory of Spintronics, School of Integrated Circuit Science and Engineering, Beihang University, Beijing 100191, China*
[4]*Institute for Theoretical Physics and Center for Extreme Matter and Emergent Phenomena, Utrecht University, Leuvenlaan 4, 3584 CE Utrecht, Netherlands*
[5]*Department of Applied Physics, Eindhoven University of Technology, P.O. Box 513, 5600 MB Eindhoven, Netherlands*
[6]*The Center for Advanced Quantum Studies, Beijing Normal University, Beijing 100191, China*

Dzyaloshinskii-Moriya interaction in magnets, which is usually derived from inversion symmetry breaking at interfaces or in noncentrosymmetric crystals, plays a vital role in chiral spintronics. Here we report that an emergent Dzyaloshinskii-Moriya interaction can be achieved in a centrosymmetric material, $La_{0.67}Sr_{0.33}MnO_3$, by a graded strain. This strain-driven Dzyaloshinskii-Moriya interaction not only exhibits distinctive two coexisting nonreciprocities of spin-wave propagation in one system, but also brings about a robust room-temperature magnetic skyrmion lattice as well as a spiral lattice at zero magnetic field. Our results demonstrate the feasibility of investigating chiral spintronics in a large category of centrosymmetric magnetic materials.

Dzyaloshinskii-Moriya interaction (DMI), an antisymmetric component of exchange interaction, was phenomenologically [1] proposed by Dzyaloshinskii and microscopically derived by Moriya by taking into spin-orbit coupling in the superexchange interaction [2]. It was initially used to explain the weak ferromagnetism in antiferromagnetic oxides and later found to be responsible for understanding a variety of physical phenomena including anisotropy fields in spin glasses [3], magnetoelectric coupling in multiferroic perovskites [4], asymmetric spin-wave dispersion [5,6] and noncollinear spin textures in chiral magnets (e.g., spin spirals [7], magnetic skyrmions [8,9], and chiral domain walls [10]), etc. Over the past decades, in addition to the noncentrosymmetric magnetic single crystals [11], DMI has been also demonstrated in thin films with asymmetric interfaces [7,12–14] or chemical composition variations [15,16], as well as in symmetric superlattices with unequally strained interfaces [17,18]. In order to further extend the material choice to explore intriguing physical phenomena for chiral spintronics, it remains highly desirable to introduce DMI into various centrosymmetric magnetic materials.

Very recently, it was proposed theoretically that strain engineering, which is able to change the crystal symmetry, could be an alternative way to generate DMI in magnetic materials belonging to centrosymmetric point groups [19].

This provides new possibilities for extending DMI to a broad set of magnetic systems [17,18]. Centrosymmetric perovskite manganites exhibit controllable structures and plenty of functionalities, such as colossal magnetoresistance [20,21], metal-insulator transition [22], and nontrivial spin textures [23–28]. Among the manganites, $La_{0.67}Sr_{0.33}MnO_3$ (LSMO) with room-temperature ferromagnetism ($T_c \sim 380$ K) and almost 100% spin polarization [29] is a prominent candidate for spintronic devices and therefore selected as a model system in this work. A strain-driven DMI is realized in the LSMO grown on $NdGaO_3$ (NGO), which is experimentally demonstrated by the frequency nonreciprocity of spin-wave propagation. By artificially engineering the epitaxial strain, room-temperature magnetic skyrmion and spiral lattices are achieved at zero magnetic field.

Bulk LSMO belongs to a symmetric trigonal crystal system with point group $\bar{3}m$ and tilted pseudocubic unit cell in which the lattice constants [30] $a_{bulk} = b_{bulk} = c_{bulk} = 3.894$ Å, and $\alpha_{bulk} \neq \beta_{bulk} = \gamma_{bulk} = 90°$, with α, β, γ being the angles between direct lattice vectors $\vec{b}$ and $\vec{c}$, $\vec{a}$ and $\vec{c}$, $\vec{a}$, and $\vec{b}$, respectively. Orthorhombic NGO (110) with a monoclinic pseudocubic lattice ($a_{NGO} = 3.855$ Å, $b_{NGO} = c_{NGO} = 3.864$ Å, $\alpha_{NGO} > \beta_{NGO} = \gamma_{NGO} = 90°$), as a substrate, provides in-plane compressive and
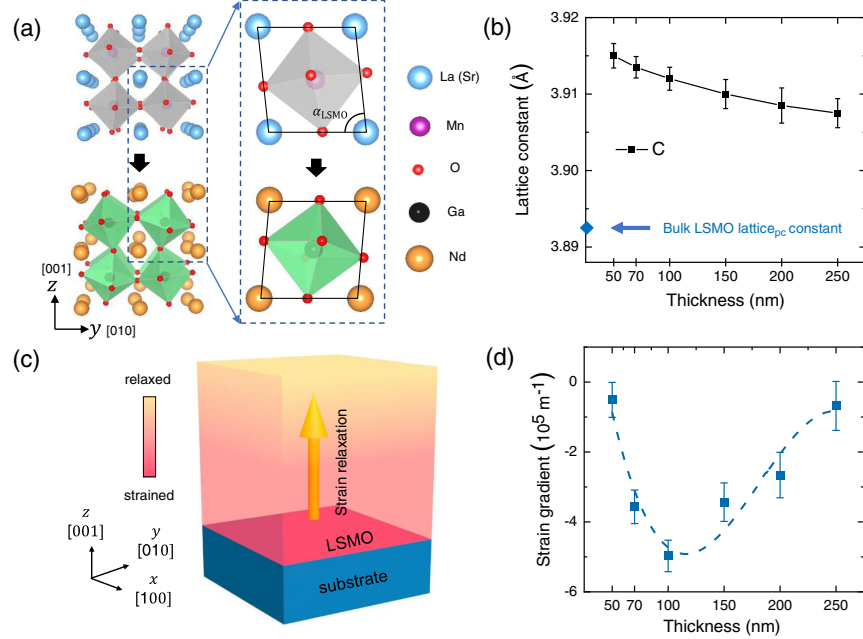
FIG. 1.   Symmetry engineering by graded strain using epitaxial growth. (a) Schematic diagram of epitaxial growth of LSMO/NGO (110) heterostructure with α being the angle of monoclinic pseudocubic lattice between b and c. (b) The c-axis lattice constant as a function of thickness with the blue arrow representing the pseudocubic (pc) lattice constant of bulk LSMO. (c) The tensile strain relaxation (yellow arrow) along out-of-plane direction. (d) Experimental estimation of tensile strain gradient which reaches maximum around 100 nm.

out-of-plane tensile strains to the LSMO film, as schematically shown in Fig. 1(a). LSMO thin films with a thickness varying from 50 to 200 nm have been grown on NGO (110) substrates by pulsed laser deposition. The detailed crystal structures have been analyzed by x-ray reciprocal space mapping and $\theta - 2\theta$ diffraction (for detail see Supplemental Material Secs. 1 and 2 [31]). The LSMO thin films on the NGO (110) substrate exhibit $2/m$ point group with monoclinic pseudocubic lattice [30], $a_{\mathrm{LSMO}} = 3.855$ Å, $b_{\mathrm{LSMO}} = 3.864$ Å, $c_{\mathrm{LSMO}} > b_{\mathrm{LSMO}} > a_{\mathrm{LSMO}}$, and $\alpha_{\mathrm{LSMO}} < \beta_{\mathrm{LSMO}} = \gamma_{\mathrm{LSMO}} = 90°$. As summarized in Fig. 1(b) and Supplemental Material Fig. S1(e) [31], the average out-of-plane lattice constant c nonlinearly decreases and the in-plane lattice constants a and b remain almost unchanged as the film thickness increases. Therefore, we conclude that the in-plane compressive strain remains unchanged whereas the out-of-plane tensile strain ε_{zz} relaxes along the z direction as schematically shown in Fig. 1(c), where the spatial variation of color stands for the strain relaxation by a finite gradient $E_{zz,z} = \partial \varepsilon_{zz} / \partial z$. The thickness dependence of the tensile strain gradient $E_{zz,z}$ is estimated from the Williamson-Hall plot [42] by $\theta - 2\theta$ x-ray diffraction (for detail, see Supplemental Material Secs. 1 and 2 [31]) and the results are summarized in Fig. 1(d). As one can see, $E_{zz,z}$ presents a nonmonotonic behavior with the increase of thickness and reaches a maximum ($\sim 5 \times 10^5$ m^{-1}) around 100 nm. The strain gradient breaks the inversion symmetry which may provide a prerequisite for the appearance of DMI [19].

To examine the existence of DMI, we measure the frequency nonreciprocity of spin-wave propagation, which is considered as an efficient method to study DMI and chiral spin structures, by utilizing vector network analyzer with integrated coplanar waveguides (CPWs) (for detail, see Supplemental Material Secs. 1 and 3 [31]). The measurements have been done in two typical configurations: an in-plane magnetic field **H** is applied to be perpendicular or parallel to the wave vector **k**, as shown in Figs. 2(a) and 2(b), respectively. During the measurements, the magnetic field $\mu_0 H = 150$ mT saturates the magnetization. Two frequency nonreciprocities $\delta f_\perp \approx 0.06$ and $\delta f_\parallel \approx 0.02$ GHz in ~ 100 nm LSMO thin film are observed for **H**$\perp$**k** [Fig. 2(c)] and **H**$\parallel$**k** [Fig. 2(d)]. Note that the amplitude difference between S_{21} and S_{12} in Fig. 2(c) reflects the nonreciprocal excitation of the Damon-Eshbach surface spin-wave mode by the antenna above the magnetic film [43]. More spectra data for different thicknesses can be found in Supplemental Material Sec. 4 [31]. As summarized in Figs. 2(e) and 2(f), both $\delta f_\perp$ and $\delta f_\parallel$ increase with thickness and reach the maximum around 100 nm, then gradually decrease. This trend is noticeably similar to the thickness dependence of the strain gradient $E_{zz,z}$ in Fig. 1(d). For a direct comparison, we replot the absolute value of $E_{zz,z}$ in Figs. 2(e) and 2(f) as the black-dashed curves. Very interestingly, the coexistence and the thickness dependence of two spin-wave nonreciprocities are in sharp contrast to previous observations [44,45], suggesting the appearance
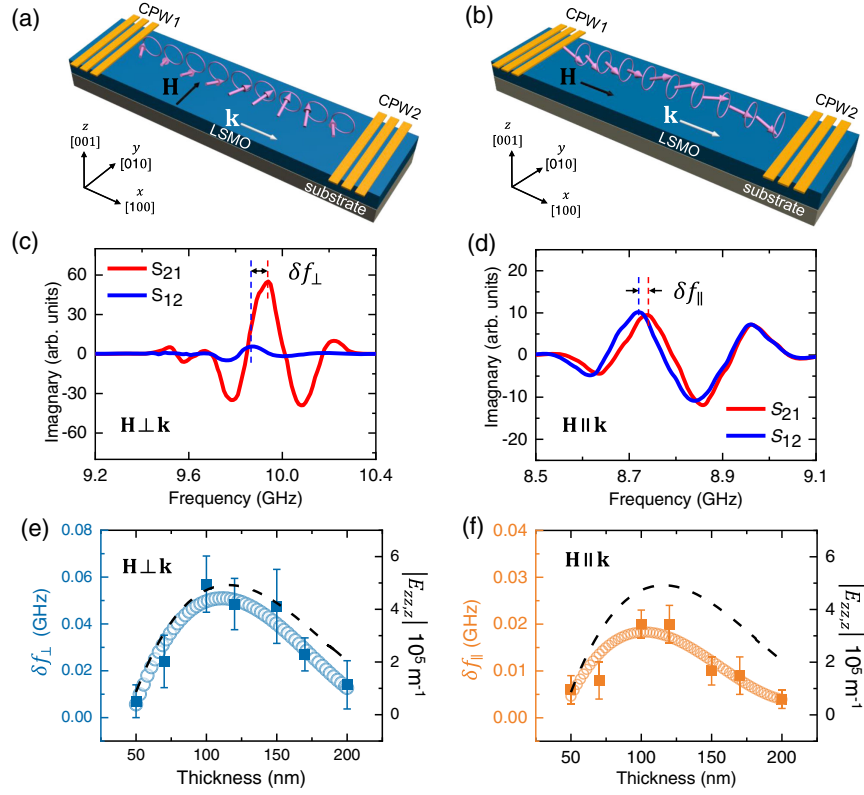
FIG. 2. Nonreciprocal spin-wave propagation. (a),(b) Setup for the measurement of nonreciprocal spin wave propagation with in-plane magnetic field (black arrows) perpendicular ($\mathbf{H}\perp\mathbf{k}$) and parallel ($\mathbf{H}\|\mathbf{k}$) to the wave vector, respectively. The wave vector $\mathbf{k}$ (white arrows) is along the x direction in all experiments and yellow antennas are coplanar waveguide (CPW1 and CPW2). (c),(d) Transmission spectra for $\mathbf{H}\perp\mathbf{k}$ and $\mathbf{H}\|\mathbf{k}$, respectively, at room temperature in 100 nm sample. S_{21} corresponds to propagating spin wave from CPW1 to CPW2, and S_{12} from CPW2 to CPW1. (e),(f) Thickness dependence of the frequency nonreciprocities in $\mathbf{H}\perp\mathbf{k}$ (blue) and $\mathbf{H}\|\mathbf{k}$ (orange), respectively. The curves of circles are fitting based on experimental data (squares). And the black-dashed curve replots the magnitude of the estimated strain gradient $E_{zz,z}$.

of an unusual DMI in this strain-driven symmetry-broken system.

For a thorough understanding and deep insight of the experimental observations, we derive the expression of this unusual DMI from thermodynamic theory description and symmetry analysis in the presence of a strain gradient $E_{zz,z}$ in our LSMO thin film [Fig. 3(a)]. According to Ref. [19], the free energy of the system consisting of coupling between magnetic order parameter (magnetization $\mathbf{m}$ and magnetization gradient $\nabla\mathbf{m}$) and strain gradient (∇E) must be an invariant of lattice symmetry of the host material, i.e., $\bar{3}m$ point group for LSMO. Detailed calculation leads to the free energy

$$f_{\text{DM}} = \sum_{i=1,2,3} \mathbf{D}_i \cdot \left(\mathbf{m} \times \frac{\partial \mathbf{m}}{\partial r_i} \right), \qquad (1)$$

where $\mathbf{D}_i = E_{zz,z}(\nu_{ix}, \nu_{iy}, \nu_{iz})$ with $i = 1, 2, 3$ represent three DM vectors for Mn-Mn pairs in [100], [010], and [001] directions, respectively, as shown by green arrows in Fig. 3(b), and ν_{ij} are the corresponding coefficients (for detail see Supplemental Material, Sec. 5 [31]).

The spin-wave nonreciprocities in the two measured configurations, i.e., $\mathbf{H}\|\mathbf{k}$ and $\mathbf{H}\perp\mathbf{k}$ are then derived from the Landau-Lifshitz equation, where the equilibrium magnetization $\mathbf{m}$ is set to be along the strong external magnetic field $\mathbf{H}$. It turns out that the resonant frequencies in the two configurations can be expressed as

$$f_{\|}(k, \pm H) = \frac{\gamma\mu_0}{2\pi}\sqrt{(Jk^2 - \xi + H + M_s)(Jk^2 + H)}$$
$$\mp \frac{\gamma k}{\pi M_s}D_{1x}, \qquad (2)$$

$$f_{\perp}(k, \pm H) = \frac{\gamma\mu_0}{2\pi}\sqrt{(Jk^2 - \xi + H + M_s)(Jk^2 + \xi + H)}$$
$$\mp \frac{\gamma k}{\pi M_s}D_{1y}, \qquad (3)$$

where $J = 2A/\mu_0 M_s$ and $\xi = \{[M_s(1 - e^{-2|k|d})]/4\}$ with A being the exchange constant, M_s saturated magnetization, μ_0 vacuum permeability, d the thickness, and γ the gyromagnetic ratio. The spin-wave nonreciprocities in frequency from DMI thus are given by
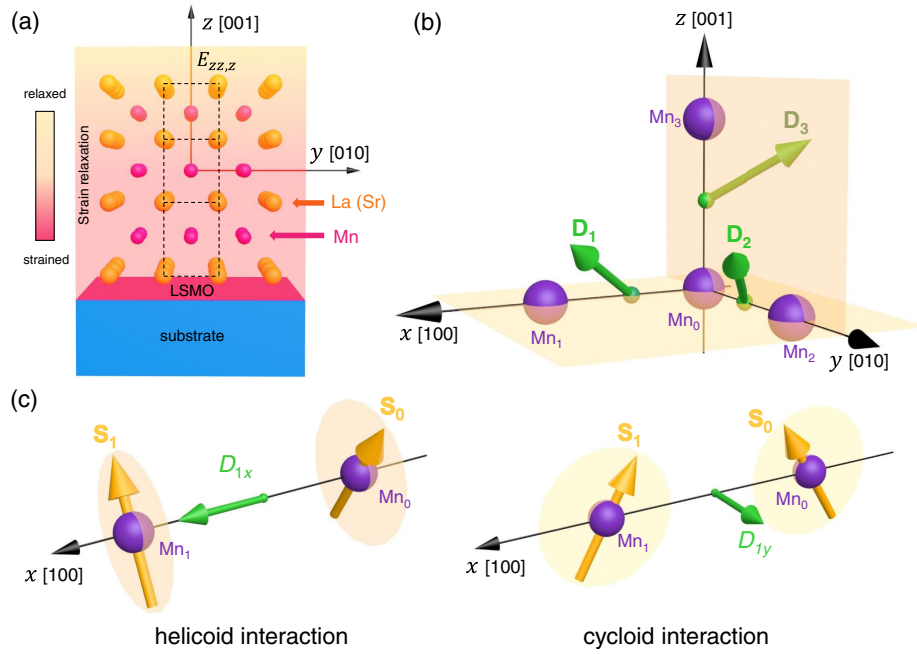
FIG. 3.   Strain-driven Dzyaloshinskii-Moriya interaction. (a) Side view of the graded lattice (black-dashed line) of a LSMO thin film with a strain gradient $E_{zz,z}$. The yellow spheres are La or Sr cations and violet spheres are Mn cations. (b) General picture of the strain-driven DMI with three DM vectors (green arrows), $\mathbf{D}_1$, $\mathbf{D}_2$, and $\mathbf{D}_3$ for Mn-Mn pairs in x, y, and z directions, respectively. (c) The two components D_{1x} and D_{1y} for different characterizations, i.e., helicoid interaction and cycloid interaction, respectively. For the spin wave propagating in the x direction, neighboring spins $\mathbf{S}_0$ and $\mathbf{S}_1$ (yellow arrows) of Mn ions rotate helicoidally (cyclodially) in the yz (xz) plane. Those two different characterizations induce the coexistence of frequency nonreciprocities in both configurations of Figs. 2(a) and 2(b).
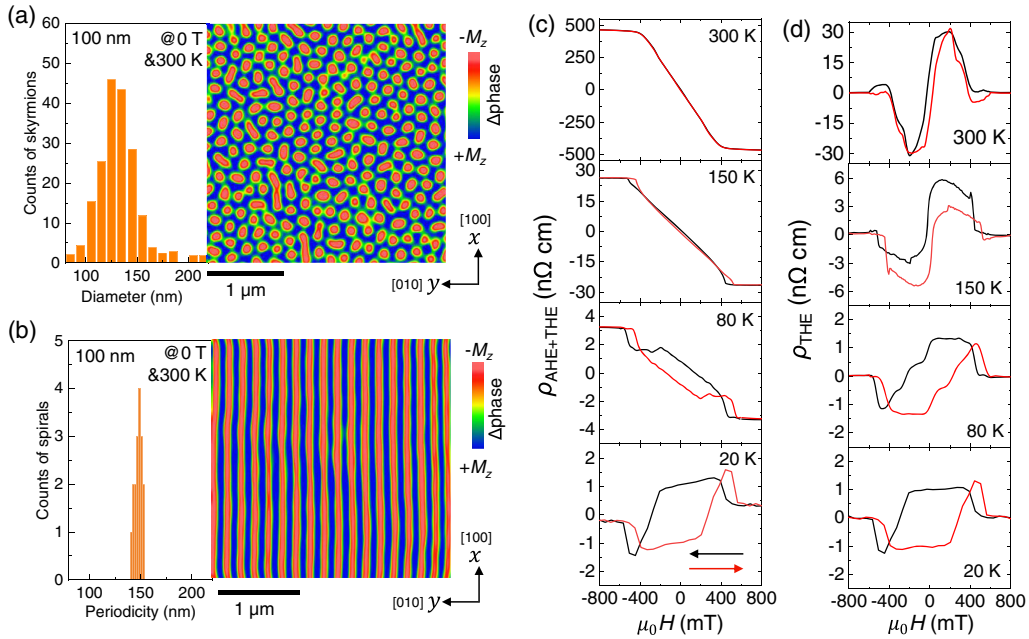

FIG. 4.   Topological spin textures at room temperature and topological Hall effect. The zero-field (a) magnetic skyrmion lattice and (b) spin-spiral lattice at room temperature for 100 nm sample. (c) Total Hall resistivity curves of AHE and THE and (d) the net THE contribution as a function of magnetic field at different temperatures. The black and red colors represent the two field-sweeping directions indicated by the colored arrows.

$$\delta f_\| = f_\|(k, H) - f_\|(k, -H) = -2k\gamma D_{1x}/\pi M_s, \quad (4)$$

$$\delta f_\perp = f_\perp(k, H) - f_\perp(k, -H) = -2k\gamma D_{1y}/\pi M_s. \quad (5)$$

In practice, the x and y components of the DMI vector for Mn_0-Mn_1 pair, D_{1x} and D_{1y}, display two different characterizations of helicoid- and cycloid-type interactions [46] as illustrated in Fig. 3(c), and hence result in the spin-wave nonreciprocities for $\mathbf{H}\|\mathbf{k}$ and $\mathbf{H}\perp\mathbf{k}$, respectively, which is well consistent with our experimental observations.

The frequency nonreciprocity due to other possible origins such as surface anisotropy [47] and magnetization gradient [37] along growth direction has been carefully studied and excluded: (1) as for surface anisotropy, the sign change of nonreciprocity from calculation does not agree with the observed nonmonotonic thickness dependence; (2) as for the magnetization gradient, no nonreciprocity is allowed for $\mathbf{H}\|\mathbf{k}$ (for detail see Supplemental Material Sec. 6 [31]). In addition, the thickness dependence of the nonreciprocity observed for $\mathbf{H}\perp\mathbf{k}$ does not coincide with the one induced by interfacial DMI (a rapid decay within a few nanometers [45]). Therefore, we conclude that the observed unusual nonreciprocity originates from the strain-driven DMI. The approach for a quantitative estimation of the DMI vector is explained in Supplemental Material Sec. 7 [31].

To further confirm the existence of the strain-driven DMI, the consequent spin textures have been directly imaged in the LSMO films by magnetic force microscopy (MFM), as the DMI may generate topological spin textures such as skyrmions and spin spirals. As shown in Figs. 4(a) and 4(b), two stable spin textures, i.e., a skyrmion lattice and a periodic spiral lattice are observed at 300 K in the 100 nm thin film (for detail see Supplemental Material Sec. 1 [31]). The topological characteristic of the spin textures is evidenced by the topological Hall effect (THE) [48,49] extracted from Hall measurements. The measured Hall resistivity ρ_{Hall} contains three contributions: normal Hall effect (NHE), anomalous Hall effect (AHE), and THE, i.e., $\rho_{Hall} = \rho_{NHE} + \rho_{AHE} + \rho_{THE}$. NHE and AHE are proportional to the out-of-plane magnetic field and magnetization, respectively. Therefore ρ_{Hall} is subtracted by $\rho_{NHE} = R_0 H$ [Fig. 4(c)] and $\rho_{AHE} = R_s M$. The net THE signals are plotted in Fig. 4(d) (for details see Supplemental Material Sec. 8 [31]). It is well known that the topological Hall resistivity due to skyrmions can be expressed as $\rho_{THE} = P R_0 n_{sk} \varphi_0$, where P is the spin polarization, R_0 the normal Hall coefficient, n_{sk} skyrmion density, $\varphi_0 = h/e$, h the Planck constant, and e the elementary charge. Taking $n_{sk} = 25 \ \mu m^{-2}$ obtained from Fig. 4(a), $P = 1$ and $R_0 = 0.0996 \ \mu\Omega\,cm\,T^{-1}$ to estimate, the topological Hall resistivity ρ_{THE} 10 nΩ cm shows reasonable agreement with the experimental value at zero magnetic field and 300 K in Fig. 4(d). Such a topological nature maintains within a wide temperature down to 20 K, where the formation, evolution, and annihilation of skyrmions match well with the field dependence of topological Hall resistivity (for details see Supplemental Material Sec. 9 [31]). The role of the DMI
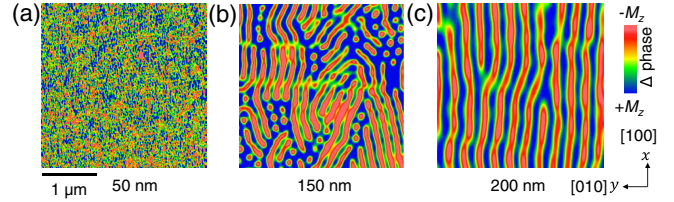

FIG. 5. Zero-field MFM images in 50, 150, and 200 nm thin film at room temperature. (a) Tiny wormlike textures in 50 nm thin film. (b) Mixed phase with a few isolated skyrmions in 150 nm thin film. (c) Spin-spiral lattice in 200 nm thin film.

strength can be seen in Fig. 5, which shows, in samples with relative weak DMI, only tiny wormlike textures or spin spirals (with larger period in weaker DMI sample, see Supplemental Material Sec. 10 [31]) can be achieved at zero field. Topological characteristic of these low-field spin textures is evidenced by nonzero topological Hall resistivities [40], see Supplemental Material Sec. 11 [31]. Thus, we demonstrate that the strain engineering is an efficient way to generate DMI and hence allows for the stabilization of zero-field nontrivial magnetic topological phase in LSMO thin films.

In summary, we report an emergent DMI in LSMO thin films, where the inversion symmetry is broken by a graded strain. Based on thermodynamic theory description and symmetry analysis, we show that the strain gradient can give rise to an unusual DMI containing both helicoid- and cycloid-type components. This strain-driven DMI stabilizes magnetic skyrmion and spin spiral lattices at room temperature and zero magnetic field. The artificial strain engineering, a well-established technique in semiconductor [50] and ferroelectric [42] communities, provides a novel strategy to explore DMI in centrosymmetric materials for the applications in spintronic devices. Discovery of a topological spin structure in this strongly correlated oxide may trigger more intriguing physical phenomena and functionalities.

Jinxing Z., K. S., and Y. Z. conceived the project and directed the research; Y. Z. and J. W. are responsible for the thin films' fabrication and strain gradient estimations; Jie L. and K. S. performed thermodynamic theory description and symmetry analysis; Y. D. and Z. L. performed all x-ray diffractions and crystal structures analysis; Y. Z. and S. W. performed magnetism and transport measurement; Jianyu

*These authors contributed equally to this work.
†Corresponding author.
 haiming.yu@buaa.edu.cn
‡Corresponding author.
 zlluo@ustc.edu.cn
§Corresponding author.
 kashen@bnu.edu.cn
‖Corresponding author.
 jxzhang@bnu.edu.cn

[1] I. Dzyaloshinsky, J. Phys. Chem. Solids **4**, 241 (1958).
[2] T. Moriya, Phys. Rev. **120**, 91 (1960).
[3] A. Fert and P. M. Levy, Phys. Rev. Lett. **44**, 1538 (1980).
[4] I. A. Sergienko and E. Dagotto, Phys. Rev. B **73**, 094434 (2006).
[5] L. Udvardi and L. Szunyogh, Phys. Rev. Lett. **102**, 207204 (2009).
[6] K. Zakeri, Y. Zhang, J. Prokop, T. H. Chuang, N. Sakr, W. X. Tang, and J. Kirschner, Phys. Rev. Lett. **104**, 137203 (2010).
[7] M. Bode, M. Heide, K. von Bergmann, P. Ferriani, S. Heinze, G. Bihlmayer, A. Kubetzka, O. Pietzsch, S. Blügel, and R. Wiesendanger, Nature (London) **447**, 190 (2007).
[8] W. Jiang et al., Science **349**, 283 (2015).
[9] S. Muhlbauer, B. Binz, F. Jonietz, C. Pfleiderer, A. Rosch, A. Neubauer, R. Georgii, and P. Boni, Science **323**, 915 (2009).
[10] K. S. Ryu, L. Thomas, S. H. Yang, and S. Parkin, Nat. Nanotechnol. **8**, 527 (2013).
[11] K. Shibata et al., Nat. Nanotechnol. **10**, 589 (2015).
[12] A. R. Fert, Mater. Sci. Forum **59–60**, 439 (1990).
[13] S. Heinze, K. von Bergmann, M. Menzel, J. Brede, A. Kubetzka, R. Wiesendanger, G. Bihlmayer, and S. Blugel, Nat. Phys. **7**, 713 (2011).
[14] N. Romming, C. Hanneken, M. Menzel, J. E. Bickel, B. Wolter, K. von Bergmann, A. Kubetzka, and R. Wiesendanger, Science **341**, 636 (2013).
[15] G. Chen et al., Sci. Adv. **6**, eaba4924 (2020).
[16] D. H. Kim et al., Nat. Mater. **18**, 685 (2019).
[17] A. V. Davydenko, A. G. Kozlov, A. G. Kolesnikov, M. E. Stebliy, G. S. Suslin, Y. E. Vekovshinin, A. V. Sadovnikov, and S. A. Nikitov, Phys. Rev. B **99**, 014433 (2019).
[18] W. Zhang, R. Chen, B. Jiang, X. Zhao, W. Zhao, S. S. Yan, G. Han, S. Yu, G. Liu, and S. Kang, Nanoscale **13**, 2665 (2021).
[19] D. A. Kitchaev, I. J. Beyerlein, and A. Van der Ven, Phys. Rev. B **98**, 214414 (2018).
[20] S. Jin, T. Tiefel, M. McCormack, R. Fastnacht, R. Ramesh, and L. Chen, Science **264**, 413 (1994).
[21] A. Urushibara, Y. Moritomo, T. Arima, A. Asamitsu, G. Kido, and Y. Tokura, Phys. Rev. B **51**, 14103 (1995).
[22] Z. Liao et al., Nat. Mater. **15**, 425 (2016).
[23] T. Nagai, M. Nagao, K. Kurashima, T. Asaka, W. Zhang, and K. Kimoto, Appl. Phys. Lett. **101**, 162401 (2012).
[24] A. Kotani, H. Nakajima, K. Harada, Y. Ishii, and S. Mori, Phys. Rev. B **94**, 024407 (2016).
[25] X. Yu, Y. Tokunaga, Y. Taguchi, and Y. Tokura, Adv. Mater. **29**, 1603958 (2017).
[26] M. Nakamura, D. Morikawa, X. Yu, F. Kagawa, T.-h. Arima, Y. Tokura, and M. Kawasaki, J. Phys. Soc. Jpn. **87**, 074704 (2018).
[27] A. Kotani, H. Nakajima, Y. Ishii, K. Harada, and S. Mori, AIP Adv. **6**, 056403 (2016).
[28] J. Fan et al., J. Magn. Magn. Mater. **483**, 42 (2019).
[29] M. Bowen, M. Bibes, A. Barthélémy, J. P. Contour, A. Anane, Y. Lemaître, and A. Fert, Appl. Phys. Lett. **82**, 233 (2003).
[30] A. Vailionis, H. Boschker, W. Siemons, E. P. Houwman, D. H. A. Blank, G. Rijnders, and G. Koster, Phys. Rev. B **83**, 064101 (2011).
[31] See Supplemental Material at http://link.aps.org/supplemental/10.1103/PhysRevLett.127.117204 for Sec. 1: method; Sec. 2: structural characterizations, estimation of strain gradient based on Williamson-Hall plot in [32–35]; Sec. 3: setup of integrated coplanar waveguides antennas; Sec. 4: raw spin-wave spectra for $\mathbf{H}\|\mathbf{k}$ configuration; Sec. 5: thermodynamic description and symmetry analysis based in [19], magnetic dipole field based in [36]; Sec. 6: analysis of frequency nonreciprocity due to surface anisotropy and magnetization gradient based in [37]; Sec. 7: quantitative estimation of the DMI vector [38]; Sec. 8: characterizations of transport and magnetic properties, data analysis of Hall transports based in [39]; Sec. 9: field-dependent magnetic force microscopy [40]; Sec. 10: spin-spiral period analysis [41]; Sec. 11: THE traces of thin films with different DMI.
[32] G. Catalan, B. Noheda, J. McAneney, L. J. Sinnamon, and J. M. Gregg, Phys. Rev. B **72**, 020102(R) (2005).
[33] D. Sando et al., Phys. Rev. Mater. **3**, 104404 (2019).
[34] X. Yu et al., Phys. Rev. B **100**, 104405 (2019).
[35] G. K. Williamson and W. H. Hall, Acta Metall. **1**, 22 (1953).
[36] R. L. Stamps, Phys. Rev. B **49**, 339 (1994).
[37] R. A. Gallardo, P. Alvarado-Seguel, T. Schneider, C. Gonzalez-Fuentes, A. Roldán-Molina, K. Lenz, J. Lindner, and P. Landeros, New J. Phys. **21**, 033026 (2019).
[38] S. R. Bakaul, W. Hu, T. Wu, and T. Kimura, Phys. Rev. B **86**, 184404 (2012).
[39] L. Vistoli et al., Nat. Phys. **15**, 67 (2019).
[40] M. Raju, A. Yagil, A. Soumyanarayanan, A. K. C. Tan, A. Almoalem, F. Ma, O. M. Auslaender, and C. Panagopoulos, Nat. Commun. **10**, 696 (2019).
[41] O. Janson, I. Rousochatzakis, A. A. Tsirlin, M. Belesi, A. A. Leonov, U. K. Rossler, J. van den Brink, and H. Rosner, Nat. Commun. **5**, 5376 (2014).
[42] B. C. Jeon, D. Lee, M. H. Lee, S. M. Yang, S. C. Chae, T. K. Song, S. D. Bu, J.-S. Chung, J.-G. Yoon, and T. W. Noh, Adv. Mater. **25**, 5643 (2013).
[43] T. An et al., Nat. Mater. **12**, 549 (2013).
[44] S. Seki et al., Phys. Rev. B **93**, 235131 (2016).
[45] J. M. Lee, C. Jang, B. C. Min, S. W. Lee, K. J. Lee, and J. Chang, Nano Lett. **16**, 62 (2016).

[46] A. N. Bogdanov, U. K. Rößler, M. Wolf, and K. H. Müller, Phys. Rev. B **66**, 214410 (2002).

[47] O. Gladii, M. Haidar, Y. Henry, M. Kostylev, and M. Bailleul, Phys. Rev. B **93**, 054430 (2016).

[48] P. Bruno, V. K. Dugaev, and M. Taillefumier, Phys. Rev. Lett. **93**, 096806 (2004).

[49] D. Maccariello, W. Legrand, N. Reyren, K. Garcia, K. Bouzehouane, S. Collin, V. Cros, and A. Fert, Nat. Nanotechnol. **13**, 233 (2018).

[50] Y. Kato, R. C. Myers, A. C. Gossard, and D. D. Awschalom, Nature (London) **427**, 50 (2004).